

Ultrafast carrier-lattice interactions and interlayer modulations of Bi₂Se₃ by X-ray free electron laser diffraction

Sungwon Kim

Sogang University

Youngsam Kim

Yonsei University

Jaeseung Kim

Sogang University

Sungwook Choi

Sogang University

Kyuseok Yun

Sogang University

Dongjin Kim

Sogang University

Soo Yeon Lim

Sogang University

Sunam Kim

PAL-XFEL, Pohang Accelerator Lab

Sae Hwan Chun

Pohang Accelerator Laboratory

Jaeku Park

Pohang Accelerator Laboratory

Intae Eom

PAL-XFEL, Pohang Accelerator Lab

Kyung Sook Kim

Pohang Accelerator Laboratory

Tae-Yeong Koo

Pohang Accelerator Laboratory

Yunbo Ou

Massachusetts Institute of Technology <https://orcid.org/0000-0002-9350-8756>

Ferhat Katmis

Massachusetts Institute of Technology

Haidan Wen

Argonne National Laboratory <https://orcid.org/0000-0002-5427-175X>

Anthony Dichiara

Advanced Photon Source, Argonne National Laboratory

Donald Walko

Argonne National Laboratory

Eric Landahl

Department of Physics, DePaul University

Hyeonsik Cheong

Sogang University <https://orcid.org/0000-0002-2347-4044>

Eunji Sim

Yonsei University

Jagadeesh Moodera

Massachusetts Institute of Technology

Hyunjung Kim (✉ hkim@sogang.ac.kr)

Sogang University <https://orcid.org/0000-0001-6211-4888>

Article

Keywords: bismuth selenide, X-ray free-electron laser, carrier-lattice interactions

Posted Date: March 29th, 2021

DOI: <https://doi.org/10.21203/rs.3.rs-361382/v1>

License: © ⓘ This work is licensed under a Creative Commons Attribution 4.0 International License.

[Read Full License](#)

Ultrafast carrier-lattice interactions and interlayer modulations of Bi₂Se₃ by X-ray free electron laser diffraction

Sungwon Kim¹, Youngsam Kim², Jaeseung Kim¹, Sungwook Choi¹, Kyuseok Yun¹, Dongjin Kim¹, Soo Yeon Lim¹, Sunam Kim³, Sae Hwan Chun³, Jaeku Park³, Intae Eom³, Kyung Sook Kim³, Tae-Yeong Koo³, Yunbo Ou⁴, Ferhat Katmis⁴, Haidan Wen⁵, Anthony Dichiara⁵, Donald Walko⁵, Eric C. Landahl⁶, Hyeonsik Cheong¹, Eunji Sim², Jagadeesh Moodera^{4,7}, and Hyunjung Kim^{1*}

¹Department of Physics, Sogang University, Seoul, 04107, Korea

²Department of Chemistry, Yonsei University, Seoul, 03722, Korea

³Pohang Accelerator Laboratory, Pohang, 37673, Korea

⁴Francis Bitter Magnet Laboratory, Massachusetts Institute of Technology, Cambridge, MA 02139, USA

⁵Advanced Photon Source, Argonne National Laboratory, Argonne, IL 60439, USA

⁶Department of Physics, DePaul University, Chicago, IL 60614, USA

⁷Department of Physics, Massachusetts Institute of Technology, Cambridge, MA 02139, USA

Correspondence and requests for materials should be addressed to H.K. (hkim@sogang.ac.kr)

As a 3D topological insulator, bismuth selenide (Bi_2Se_3) has potential applications for electrically and optically controllable magnetic and optoelectronic devices. Understanding the coupling with its topological phase requires studying the interactions of carriers with the lattice on time scales down to the sub-picosecond regime. Here we use an X-ray free-electron laser to perform time-resolved diffraction to investigate the ultrafast carrier-induced lattice contractions and interlayer modulations in Bi_2Se_3 thin films. The lattice contraction depends on the carrier concentration and is followed by an interlayer expansion accompanied by oscillations. Using density functional theory (DFT) and the Lifshitz model, the initial contraction can be explained by van der Waals force modulation of the confined free carrier layers. Band inversion, related to a topological phase transition, is modulated by the expansion of the interlayer distance. These results provide insight into instantaneous topological phases on ultrafast timescales.

Bismuth selenide (Bi_2Se_3) is a well-known thermoelectric material^{1,2}, a V-VI semiconductor, and 2D van der Waals (vdW) material³ consisting of quintuple layers (QLs). As a 3D topological insulator (TI)⁴⁻⁷, Bi_2Se_3 has potential applications in optoelectronic^{8,9} and electronic devices^{4,6,10-13}, and has been extensively studied. Furthermore, new applications have been suggested for heterostructures with strong spin-orbit coupling (SOC) and spin-momentum locking¹⁴. It is therefore important to study ultrafast carrier-related intra- and inter-layer changes in the structure to manipulate the carriers in a topologically non-trivial, quasi-2D layered system^{11-13,15-17}.

Time-angle-resolved photoemission spectroscopy (trARPES) was used to study the relaxation dynamics of optically excited carriers decaying through the surface state (SS)¹⁸, as well as oscillatory modulations of the electronic structure in the bulk and SSs¹⁹. Using transient laser reflections, longitudinal optical (LO) phonons with measurable carrier relaxation times were observed during electron-LO-phonon scattering²⁰. These observations revealed a carrier relaxation mechanism representing a hybrid between one dominated by bulk polar phonon interactions and one dominated by surface electron-lattice interactions. How the carrier- Bi_2Se_3 lattice interactions couple with the vdW structures, however, needs to be investigated by direct observations. Using an X-ray free-electron laser (XFEL)²¹⁻²⁶, atomic-scale lattice movements and distortions can be measured directly on timescales down to a few tens of femtoseconds.

Here we describe the ultrafast time-resolved X-ray diffraction (UTXRD) experiment, carried out at PAL-XFEL²⁷, which studied the ultrafast carrier-induced dynamics of the Bi_2Se_3 lattice. The excited carriers induced lattice contraction that lasted up to 10 ps. Due to a confined layer of free carriers, high laser fluence may saturate the contraction. The contraction was followed by a lattice expansion that lasted tens of picoseconds and interlayer vibrations with breathing and interface modes. The vibrations were caused by modulating vdW forces restoring

the out-of-plane distortions. The carrier-induced vdW contraction was explained by density functional theory (DFT) calculations employing the Lifshitz model. We predict that an expansion in the interlayer distance will be followed by an inversion in the topologically non-trivial band state.

Figure 1a shows the (006) Bragg reflection, accumulated over 60 shots, of a Bi₂Se₃ sample with 16 QLs. Additional features can be seen, such as fringes in Q_z due to the sample thickness and diffuse scattering in Q_{xy} . The thicknesses of the sample are determined by X-ray reflectivity and by the fringes (ΔQ_z) of the (003) Bragg peak (Supplementary Fig. 1). After laser pumping, an XFEL pulse probes the structure after a time delay Δt . Figure 1b shows the time trace of the mean intensity of the in-plane ($\Delta Q_{xy} = 0.08 \text{ \AA}^{-1}$) (006) Bragg peak from Fig. 1a. The intensity profile at $\Delta t = 0$ is plotted as a blue line. To locate the Bragg peak, the signal of the crystal truncation rods was excluded from the raw data (Supplementary Fig. 2). The peak position was defined as the center of mass (COM). From this, the strain was calculated by the relation $\frac{\Delta Q}{Q_I}$, where Q_I is the initial COM at negative Δt , and ΔQ is its change after Δt . Since no changes were observed in Q_{xy} , Q_I and ΔQ are in $Q_z(\text{\AA}^{-1})$. Note that compression is defined by a positive ΔQ . The strain as a function of Δt is shown in Figs. 1c and 1d, respectively, for a 16 QL sample with different laser fluences and for samples with different thicknesses at a fixed laser fluence of 1.1 mJcm^{-2} . The inset in Fig. 1c shows the strain curves when $\Delta t > 6 \text{ ps}$ for fluences of 2.2 and 3.3 mJcm^{-2} . After laser excitation, a contractive strain was observed. The time to reach maximum contraction depended on the sample thickness and laser fluence. An expansion was then observed, followed by a relaxation with oscillations at different frequencies depending on the sample thickness.

Figures 2a and 2b show the changes in position relative to the diffraction geometry (Supplementary Fig. 3) for the (006) and (015) Bragg peaks after the laser excitation. For both peaks, the changes in Q_z were almost identical; the changes in Q_{xy} also showed no difference (Supplementary Fig. 4). We infer the possibility that a change in the interlayer distance plays a dominant role in the out-of-plane dynamics.

The oscillations and relaxations are modelled by Equation (1)

$$f_{fit} = \sum_{i=1}^m \left[A_{osc}^i e^{-t/\tau_{osc}^i} \cos 2\pi f_{osc}^i (t - \phi_i) \right] + \sum_{j=1}^l A_{rlx}^j e^{-t/\tau_{rlx}^j} \quad (1)$$

where A_{osc} , τ_{osc} , and f_{osc} are the amplitude, damping constant, and oscillation frequency for the i th component, respectively. A_{rlx} and τ_{rlx} are the relaxation amplitude and damping constant for the j th component, respectively. Figures 2c to 2f show the detailed fitting procedures and results for a 16 QL sample with 1.1 mJ/cm² laser fluence. Over the entire range $\Delta t < 400$ ps, we fit a single exponential relaxation term ($l = 1$, Fig. 2c). After subtracting this term, two superposed damping oscillations (Fig. 2d) with high ($i = 1$, Fig. 2e) and low ($i = 2$, Fig. 2f) frequencies are analysed. For an extended range of Δt , additional damping constants are needed to model the strain relaxation. Figures 2g and 2h show the damping constants τ_{rlx}^1 and τ_{rlx}^2 for both 16 and 26 QL samples, respectively. The error bars represent the 95% confidence intervals. For $\Delta t < 1,000$ ps and the 16 QL sample, the average τ_{rlx}^1 is 336 ± 36 ps. However, for $\Delta t > 1.5$ ns, i.e., when the coherent motion of the lattice diminished and thermal processes dominated, additional damping constant $\tau_{rlx}^2 = 3.66 \pm 0.29$ ns is required. The results do not change significantly with fluence. The damping constants for the 26 QL sample are greater than those for the 16 QL one, implying that thermal diffusion takes longer through the thicker sample. Results for other sample thicknesses are provided in the Supplementary Information. Figure 2i shows two distinct damping oscillation components: a

high frequency (red) and a low frequency (blue). The measurements obtained by circularly polarized Raman spectroscopy (squares) are compared to those obtained by fitting a simple linear chain (SLC) model (line). Detailed Raman spectroscopy results are provided in the Supplementary Information. The high-frequency mode is taken as the lowest frequency interlayer breathing mode in an SLC model (Fig. 2g inset). For out of plane motions, the QLs (circles) are bonded together by vdW forces with elastic constant K_z . The force constant between the QLs and the substrate is K_i . Since $K_i \ll K_z$ for 2D materials on substrates^{28,29}, the eigenmode frequencies can be written as

$$\omega_\alpha \cong \sqrt{\frac{K}{2\mu\pi^2 c^2} \left[1 - \cos\left(\frac{(\alpha-1)\pi}{N}\right) \right]} \quad (2)$$

where $\alpha = 1$ corresponds to the zero-frequency acoustic mode, and $\alpha = 2, \dots, N$ to the interlayer breathing modes when $K = K_z$. The constant c is the speed of light, and μ is $7.5 \times 10^{-6} \text{ kgm}^{-2}$ for a single QL of Bi_2Se_3 . Fitting Equation 2 to the data in Fig. 2i gives $K_z = 5.48 \times 10^{19} \text{ Nm}^{-3}$ for the breathing mode. Although $\alpha = 2$ was taken as the lowest order of the breathing modes, the low-frequency mode does not resemble the breathing or shearing modes expected in interlayer vibrations. We call this the interface mode for the following reason. Since our UTXRD measurements are sensitive to out-of-plane motions, this mode presumably represents the sample density fluctuations caused by acoustic waves at the sample-substrate interface, subjected to strong interlayer bonding ($K_z \gg K_i$). For each sample thickness, $K_i = 4(\pi c \omega_i)^2 N \mu$. The calculated (K_i/K_z) ratios shown in Table 1 are comparable to those for Bi_2Te_3 ³⁰. In Fig. 2j, the acoustic sound velocities calculated for the breathing mode are compared to the values obtained by Raman measurement³¹ (triangles), transient laser reflection³¹ (squares), and the longitudinal and transverse values (lines) calculated for the bulk³². Our results with a dependency on film thickness are consistent with those in Ref. 31.

This could be due to the coupling of the oscillations (breathing mode) and shear components with the boundary conditions³¹.

Figure 3a shows the fluence-dependent contractive strain curves ($\Delta t < 8$ ps) for the 16 QL sample described in Fig. 1c. The contractive strain data (dots) are shown with fitted error functions (lines). The maximum compression (squares) and corresponding Δt (open circles) are also shown. With fluence ~ 0.4 mJcm⁻², the contraction saturates at ($\Delta Q/Q_I \sim 0.027\%$) but is tapered during the interval Δt . After contraction, the expansion reaches a maximum at ~ 20 ps, independent of the fluence. Figure 3b shows the maximum expansive strain as a function of fluence for the same 16 QL sample. The inset shows an enlarged range of up to 0.5 mJcm⁻². Unlike compression, the expansion is linearly related to the fluence and does not saturate.

To understand how the initial compressive strain is related to the fluence-dependent carrier density (n), we calculated the latter by measuring the transmittance and reflectance values (see Supplementary Information). To determine how fluence affects the contraction time, we compared our results with those obtained in a study using time-resolved angle-resolved photoemission spectroscopy (trARPES)¹⁸ and an 800 nm fs-laser for excitation. A 26 μ Jcm⁻² fluence corresponds to 0.1 mJcm⁻² (24 μ Jcm⁻² after considering transmittance and reflectance) in our measurement. Figure 3c shows the strain curve for a fluence of 0.1 mJcm⁻². The 2.47 ps taken to reach maximum contraction is in agreement with the 2.5 ps¹⁸ taken for the carriers to completely relax by scattering from the higher-lying states, after they populated the SS and bulk conduction band (BCB) within 0.7 ps of excitation. Since the X-ray penetrate the entire 16 QLs, the SS population is negligible. The observed contractions are therefore attributed to the carriers that populated the BCB.

To relate the density of the excited carriers to the magnitude of the lattice contraction, we

used the Lifshitz model³³. By considering the dielectric function, this model explains the vdW force between metallic surfaces separated by distance (l), which is small compared to the wavelengths of the fluctuating field. We assume that the excited carriers formed a charge slab inside the QL, and each slab is separated by the distance l . At the high carrier density limit, where the plasma frequency is much larger than the Drude damping term in the dielectric function, the Drude model gives the effective pressure between charged slabs²⁶ as

$$\Delta F = \frac{\xi \hbar e \sqrt{n}}{32 \pi^2 \sqrt{2 m \epsilon_0} l^3} \quad (3)$$

where \hbar is the Planck constant, e is the elementary electron charge, ϵ_0 is the vacuum permittivity, n is the carrier density, and $\xi = 2.04$ ²⁶ is the Matsubara frequency. The stress is calculated by multiplying the elastic tensor component along the c-axis (C_{33}) by the maximum contraction in Fig. 3a. Figure 4a shows the compressive stress on the 16 QL sample (circle) as a function of n and the fit with Equation (3) (line). The distance l is 3.94 Å from the fit and is larger than the interlayer distance of Bi₂Se₃ (2.58 Å) calculated by DFT. This implies that in Bi₂Se₃, the charge density (CD) within a QL is responsible for the vdW attraction. Note that the data with $n > 3.564 \times 10^{20}$ were excluded from the fit due to saturation (inset of Fig. 4a).

After fitting Equation (3) to the data, we wanted to explore the meaning of the parameter l in a QL. Using DFT, we calculated the CD of the valence band (VB) and the conduction band (CB). The calculations are described in the Methods section. Figure 4b shows the CD and atomic configuration in a single QL along the c-axis direction. DFT geometry optimization gave the following intra-layer distances: 1.58 Å for Se(outer)–Bi, 1.90 Å for Bi–Se(inner), and 2.58 Å for the interlayer distance (s), which is the distance between Se(outer)-Se(outer) layers. The black dashed lines indicate indentations $l/2$ from each edge of the QL (9.55Å). The CD of the VB (cyan) shows electrons distributed around the Se atoms. The CD of the CB (purple) has

a distribution that is diffuse within the dashed lines and decreases sharply outwards, reaching a minimum within the interlayer distance. As the region between the dashed lines contains most of the CB carriers ($> 70\%$), we consider it as a charged slab with thickness $d = 9.55 - l$ (Å). In other words, the carriers confined within the slab (d) are responsible for the compressive strain.

To investigate how interlayer distance modulation affects the topological phase of Bi_2Se_3 ^{16,34}, we calculated the band structures for different interlayer distances ($s + \Delta s$) while keeping the atomic structure within the QL fixed. The band structure near the Γ point and corresponding projected density of states (PDOS) with interlayer distance changes (Δs in inset) are overlaid in Figure 4c. The atomic orbitals are indicated by the coloured lines. The PDOS shows that as Δs expands, p_z orbitals contribute to the inversion state, but the p_z orbital contribution remains constant regardless of inversion. According to our observations, with increasing laser fluence, the lattice expands linearly after the carrier-induced contraction. For a 3.3 mJcm^{-2} fluence, it expands to 29.43 Å , 0.79 Å larger than during the equilibrium state. We attribute most of the expansion to a coherent interlayer distance modulation since neither significant in-plane lattice change nor evidence of lattice thermalization has been observed on this time scale. In the DFT calculations, the energy gap between the inverted states narrows when the interlayer distance expands. The band is inverted when the interlayer distance expansion exceeds 0.34 Å , predicting a topological phase transition to a normal insulator. In this work, the largest observed interlayer distance expansion is 0.26 Å ; the corresponding energy band gap is 0.06 eV — a reduction of 0.24 eV compared to the equilibrium state. This suggests that the topological phase is optically tunable on an ultrafast timescale.

In conclusion, we have studied the lattice dynamics of Bi_2Se_3 on ultrafast timescales, observing the consecutive dynamical phases induced by carrier excitation. During $\Delta t < \sim 6$ ps, due to the presence of a concentrated layer of carriers within a QL, an impulsive contraction is induced by modulating vdW forces. By performing DFT calculations with the Lifshitz model, we found that the carrier layer is 5.61 Å thick, with 70% of the carriers occupying the CB. As the contraction is reversed by carrier-lattice interaction, we observed breathing and interface mode oscillations. The vibration modes of the interlayer oscillations are assigned by an SLC model. The linear relationship between the sample thickness and damping constants of the oscillations and relaxations suggests a role for thermal diffusion. The Bi_2Se_3 samples undergo maximum interlayer expansion at the beginning of the interlayer oscillations. How the topologically inverted states near the Fermi level are modulated is explained quantitatively by the expansion of the interlayer distance. With an expansion of 0.26 Å, the bulk band gap is expected to narrow to 0.06 eV. Hence a topological phase transition to a normal insulator is predicted for an expansion larger than 0.34 Å. These findings may provide insights relevant to applications that utilize the ultrafast topological states in 2D TIs.

Methods

Sample preparation

The Bi₂Se₃ films were grown on insulating Al₂O₃ (0001) substrates, along with the [001], using a molecular beam epitaxy (MBE) co-evaporation method. The ultra-high vacuum (UHV) system has a base pressure below 3.75×10^{-10} Torr. Before film growth, the substrate was cleaned with acetone and isopropyl alcohol and dried by dry nitrogen. The substrate was then loaded into a UHV system and degassed at 600°C for 10 min, and then at 800°C for 30 min. High-purity Bi (99.999%) and Se (99.999%) were co-evaporated from Knudsen cells adjusted to obtain a 2:3 compositional ratio in the grown film. Growth rates were measured by two independent *in-situ* quartz crystal monitors. The Bi₂Se₃ films were grown at a substrate temperature of 240°C under Se-rich conditions, with a typical Se/Bi flux ratio of 10. The typical growth rate was 1 QL min⁻¹ (QL, where 1 QL \approx 0.96 nm). A protective 5-nm amorphous Al₂O₃ layer was then deposited *in-situ* at room temperature.

X-ray reflectivity measurements

X-ray reflectivity measurements were taken with a D8 Discover diffractometer (Bruker Corporation, Billerica, MA, USA). An 8.05 keV (Cu K_α) X-ray beam was collimated by a Göbel mirror and then filtered by a Ni filter to exclude the K_β emission.

Ultrafast time-resolved X-ray diffraction

With a 500-fs time resolution and delays up to hundreds of ps, the UTXRD measurements were carried out at the X-ray Scattering and Spectroscopy (XSS) beamline at PAL-XFEL

(Pohang, Korea)³⁵. A monochromatized X-ray pulse with a pulse duration of ~ 20 fs was used to probe the sample at a time delay Δt after the optical laser pump. The Si(111) double crystal monochromator was operated at 9.7 keV with $\Delta E/E \sim 1.6 \times 10^{-4}$. The X-ray pulses were focused by beryllium compound refractive lenses (CRL) to a spot of size of $20 \times 20 \mu\text{m}^2$ full width at half maximum (FWHM) at the sample location. A Ti:sapphire laser with 800 nm wavelength and pulse width of 100 fs FWHM was used as the optical pump. It was p-polarized to the sample surface, and its angle of incidence was 9.6° larger than the X-ray. The laser provided effective fluences between 0.1 and 3.3 mJcm^{-2} on the sample surface. After a time delay Δt , measurements were taken with the laser on and off, and then compared. The X-ray scattering patterns were recorded by a 2D “multiport charged-coupled device” (MPCCD) with a 10–30 Hz frequency.

Time-resolved X-ray diffraction measurements with delays of up to 8 ns were taken at the 7-ID-C beamline of the Advanced Photon Source (USA). A Ti:sapphire laser with 50 fs FWHM pulse duration, 800 nm wavelength, and 1 kHz repeating frequency was used as the optical pump. The sample was probed by 10 keV X-ray pulses with an FWHM duration of 90 ps. Collinear with the X-ray beam, the pump laser gave fluences between 0.7 and 8.8 mJcm^{-2} at the sample surface. A 2D Pilatus detector was used 1 m from the sample.

Density functional theory (DFT) calculations

The electronic structure of Bi_2Se_3 was calculated using DFT at the level of the generalized gradient approximation (GGA), in particular, Perdew-Burke-Ernzerhof (PBE)³⁶ functional including spin-orbit coupling (SOC) implemented in the Vienna Ab Initio Simulation Package (VASP)³⁷. The projector augmented wave (PAW) method³⁸ was used in the calculations.

Specifically, $5s$, $6s$, $5p$, $6p$, and $5d$ of bismuth, and $4s$ and $4p$ of selenium, were included as the valence states. The convergence criterion for the self-consistency calculation was 10^{-6} eV, and the kinetic energy cut-off was 340 eV with accurate precision mode. The Brillouin zone was sampled using $13 \times 13 \times 13$ k-points according to the Monkhorst-Pack scheme. The tetrahedron method with Blöchl corrections was used, except for the band structure calculations.

To optimize the geometry, we fixed the lattice constants of a hexagonal unit cell and released the atomic positions. The in-plane lattice parameters “a” and “c” were set to 4.17 \AA^{17} and 28.64 \AA^{39} , respectively. The optimization procedure continued until the Hellmann-Feynman forces became smaller than 0.01 eV/\AA , and the vdW interactions between the QLs could be taken into account by Grimme’s vdW correction (D2)⁴⁰.

The CD distribution in the z-direction (Fig. 4b) was obtained based on the local integral curve using Multiwfn⁴¹. The curve is defined as $I_L(z) = \int \int p(x, y, z) \, dx dy$. We summed the charge densities of the carriers in the VB and CB near the Γ point. The k-points contained $1/4$ of the $\Gamma \rightarrow M$, $\Gamma \rightarrow K$ and $\Gamma \rightarrow A$ paths.

The band structure (Fig. 4c) was calculated, as well as the symmetry points (K, Γ , M). With Gaussian smearing (0.01 eV broadening), each line contained 80 such points. Various structures in the interlayer distance were calculated while keeping the atomic structure within a QL fixed. We obtained the PDOS at the Γ point by incorporating the lm -decomposed scheme into the band structure calculation.

References

1. Mishra, S. K., Satpathy, S. & Jepsen, O. Electronic structure and thermoelectric properties of bismuth telluride and bismuth selenide. *J. Phys. Condens. Matter* **9**, 461–470 (1997).
2. Ghaemi, P., Mong, R. S. K. & Moore, J. E. In-plane transport and enhanced thermoelectric performance in thin films of the topological insulators Bi_2Te_3 and Bi_2Se_3 . *Phys. Rev. Lett.* **105**, 166603 (2010).
3. Geim, A. K. & Grigorieva, I. V. Van der Waals heterostructures. *Nature* **499**, 419–425 (2013).
4. Zhang, H. *et al.* Topological insulators in Bi_2Se_3 , Bi_2Te_3 and Sb_2Te_3 with a single Dirac cone on the surface. *Nat. Phys.* **5**, 438–442 (2009).
5. Moore, J. E. The birth of topological insulators. *Nature* **464**, 194–198 (2010).
6. Qi, X. L. & Zhang, S. C. Topological insulators and superconductors. *Rev. Mod. Phys.* **83**, 1057–1110 (2011).
7. Fu, L., Kane, C. L. & Mele, E. J. Topological insulators in three dimensions. *Phys. Rev. Lett.* **98**, 106803 (2007).
8. Zhang, H., Zhang, X., Liu, C., Lee, S. T. & Jie, J. High-Responsivity, High-Detectivity, Ultrafast Topological Insulator Bi_2Se_3 /Silicon Heterostructure Broadband Photodetectors. *ACS Nano* **10**, 5113–5122 (2016).
9. Wang, F. *et al.* Submillimeter 2D Bi_2Se_3 Flakes toward High-Performance Infrared Photodetection at Optical Communication Wavelength. *Adv. Funct. Mater.* **28**, 1802707

- (2018).
10. Mellnik, A. R. *et al.* Spin-transfer torque generated by a topological insulator. *Nature* **511**, 449–451 (2014).
 11. Luo, L. *et al.* Ultrafast manipulation of topologically enhanced surface transport driven by mid-infrared and terahertz pulses in Bi₂Se₃. *Nat. Commun.* **10**, 607 (2019).
 12. Checkelsky, J. G., Hor, Y. S., Cava, R. J. & Ong, N. P. Bulk band gap and surface state conduction observed in voltage-tuned crystals of the topological insulator Bi₂Se₃. *Phys. Rev. Lett.* **106**, 196801 (2011).
 13. Kim, D. *et al.* Surface conduction of topological Dirac electrons in bulk insulating Bi₂Se₃. *Nat. Phys.* **8**, 459–463 (2012).
 14. Katmis, F. *et al.* A high-temperature ferromagnetic topological insulating phase by proximity coupling. *Nature* **533**, 513–516 (2016).
 15. Flötotto, D. *et al.* In Situ Strain Tuning of the Dirac Surface States in Bi₂Se₃ Films. *Nano Lett.* **18**, 5628–5632 (2018).
 16. Aramberri, H. & Muñoz, M. C. Strain-driven tunable topological states in Bi₂Se₃. *J. Phys.: Mater.* **1**, 015009 (2018).
 17. Hsieh, D. *et al.* A tunable topological insulator in the spin helical Dirac transport regime. *Nature* **460**, 1101–1105 (2009).
 18. Sobota, J. A. *et al.* Ultrafast optical excitation of a persistent surface-state population in the topological insulator Bi₂Se₃. *Phys. Rev. Lett.* **108**, 117403 (2012).
 19. Sobota, J. A. *et al.* Distinguishing bulk and surface electron-phonon coupling in the

- topological insulator Bi₂Se₃ using time-resolved photoemission spectroscopy. *Phys. Rev. Lett.* **113**, 117401 (2014).
20. Glinka, Y. D. *et al.* Ultrafast carrier dynamics in thin-films of the topological insulator Bi₂Se₃. *Appl. Phys. Lett.* **103**, 151903 (2013).
 21. Trigo, M. *et al.* Fourier-transform inelastic X-ray scattering from time- and momentum-dependent phonon-phonon correlations. *Nat. Phys.* **9**, 790–794 (2013).
 22. Zhu, D. *et al.* Phonon spectroscopy with sub-meV resolution by femtosecond x-ray diffuse scattering. *Phys. Rev. B* **92**, 054303-1 (2015).
 23. Fritz, D. M. Ultrafast bond softening in Bismuth : *Science* **315**, 633–637 (2007).
 24. Zalden, P. *et al.* Femtosecond x-ray diffraction reveals a liquid–liquid phase transition in phase-change materials. *Science* **364**, 1062–1067 (2019).
 25. Lindenberg, A. M., Johnson, S. L. & Reis, D. A. Visualization of atomic-scale motions in materials via femtosecond X-ray scattering techniques. *Annu. Rev. Mater. Res.* **47**, 425–449 (2017).
 26. Mannebach, E. M. *et al.* Dynamic optical tuning of interlayer interactions in the transition metal dichalcogenides. *Nano Lett.* **17**, 7761–7766 (2017).
 27. Kang, H. S. *et al.* Hard X-ray free-electron laser with femtosecond-scale timing jitter. *Nat. Photonics* **11**, 708–713 (2017).
 28. Tan, P. H. *et al.* The shear mode of multilayer graphene. *Nat. Mater.* **11**, 294–300 (2012).
 29. Zhao, Y. *et al.* Interlayer breathing and shear modes in few-trilayer MoS₂ and WSe₂. *Nano Lett.* **13**, 1007–1015 (2013).

30. Zhao, Y. *et al.* Interlayer vibrational modes in few-quintuple-layer Bi₂Te₃ and Bi₂Se₃ two-dimensional crystals: Raman spectroscopy and first-principles studies. *Phys. Rev. B* **90**, 245428 (2014).
31. Glinka, Y. D., Babakiray, S., Johnson, T. A., Holcomb, M. B. & Lederman, D. Acoustic phonon dynamics in thin-films of the topological insulator Bi₂Se₃. *J. Appl. Phys.* **117**, 165703 (2015).
32. Giraud, S., Kundu, A. & Egger, R. Electron-phonon scattering in topological insulator thin films. *Phys. Rev. B.* **85**, 035441 (2012).
33. Lifshitz, E. M. The theory of molecular attractive forces between solids. *Perspect. Theor. Phys.* **2**, 329–349 (1992).
34. Yang, W. J. *et al.* Tuning of topological Dirac states via modification of van der Waals gap in strained ultrathin Bi₂Se₃ films. *J. Phys. Chem. C* **122**, 23739–23748 (2018).
35. Park, J. *et al.* Design of a hard X-ray beamline and end-station for pump and probe experiments at Pohang Accelerator Laboratory X-ray Free Electron Laser facility. *Nucl. Instruments Methods Phys. Res. Sect. A Accel. Spectrometers, Detect. Assoc. Equip.* **810**, 74–79 (2016).
36. Kresse, G. & Furthmüller, J. Efficient iterative schemes for ab initio total-energy calculations using a plane-wave basis set. *Phys. Rev. B* **54**, 11169–11186 (1996).
37. Perdew, J. P., Burke, K. & Ernzerhof, M. Generalized gradient approximation made simple. *Phys. Rev. Lett.* **77**, 3865–3868 (1996).
38. Blöchl, P. E. Projector augmented-wave method. *Phys. Rev. B* **50**, 17953–17979 (1994).

39. Lind, H., Lidin, S. & Häussermann, U. Structure and bonding properties of $(\text{Bi}_2\text{Se}_3)_m(\text{Bi}_2)_n$ stacks by first-principles density functional theory. *Phys. Rev. B - Condens. Matter Mater. Phys.* **72**, 184101 (2005).
40. Allouche, A. Semiempirical GGA-Type Density Functional Constructed with a Long-Range Dispersion Correction. *J. Comput. Chem.* **27**, 1787–1799 (2006).
41. Lu, T. & Chen, F. Multiwfn: A multifunctional wavefunction analyzer. *J. Comput. Chem.* **33**, 580–592 (2012).

ACKNOWLEDGEMENTS

We thank Sanghoon Song and Aymeric Robert for fruitful discussions. This research was supported by the National Research Foundation of Korea (NRF-2015R1A5A1009962, 2019R1A6B2A02100883). Y.K. and E.S. acknowledge the support from NRF-2020R1A2C2007468. Use of the Advanced Photon Source was supported by the Office of Basic Energy Science, under the Office of Science of the US Department of Energy (Contract No. DE-AC02-06CH11357). The experiments were carried out at the XSS beamline of PAL-XFEL (experiment no. 2017-1st-FXS-006 and 2018-1st-XSS-010) funded by the Ministry of Science and ICT of Korea. The work at MIT was supported by the Center for Integrated Quantum Materials (NSF-DMR 1231319), the NSF Grant DMR 1700137, NSF CONVERGENCE ACCELERATOR TRACK C: SYN OIA-2040620, and ONR Grants N00014-16-1-2657 and N00014-20-1-2306.

Corresponding author

Correspondence to: Hyunjung Kim

Author contributions

H.K. supervised and coordinated all aspects of the project. The UTXRD measurements at PAL-XFEL were carried out by S.K., J.K., S.C., K.Y., D.K., S.K., S.H.C., J.P., I.E., K.K, T-Y.K., and H.K. The UTXRD measurements at APS were carried out by S.K., K.Y., H.W., A.D., D.W., E.C.L., and H.K. The UTXRD data were analysed by S.K. The Bi₂Se₃ thin films were grown by Y.O. and F.K. under the supervision of J.S.M. The XRR measurements were carried out by J.K. and S.K. The theoretical analyses and density functional theory calculations were carried out by S.K. and Y.K., under the supervision of E.S. and H.K. S.Y.L. carried out the Raman spectroscopic measurements under the supervision of H.C. S.K., Y.K., E.S., and H.K. wrote the paper. All authors discussed the results and commented on the manuscript.

Figure 1. Strain evolution observed at the (006) Bragg peak. (a) The (006) Bragg reflection before laser excitation. (b) In-plane ($\Delta Q_{xy} = 0.08 \text{ \AA}^{-1}$)-averaged (006) Bragg peak after the time delay. The intensity profile at $\Delta t = 0$ is indicated by the blue line. (c) Strain evolution in a 16 QL Bi_2Se_3 film for different laser fluences. Contractive strains are observed between time delays of 0 and 6 ps. The lattice is subsequently released, and the strain rapidly turns expansive and is accompanied by oscillations. (d) Strain evolution in Bi_2Se_3 films with 7, 16, 26, 43, and 78 QLs, at 1.1 mJcm^{-2} fluence.

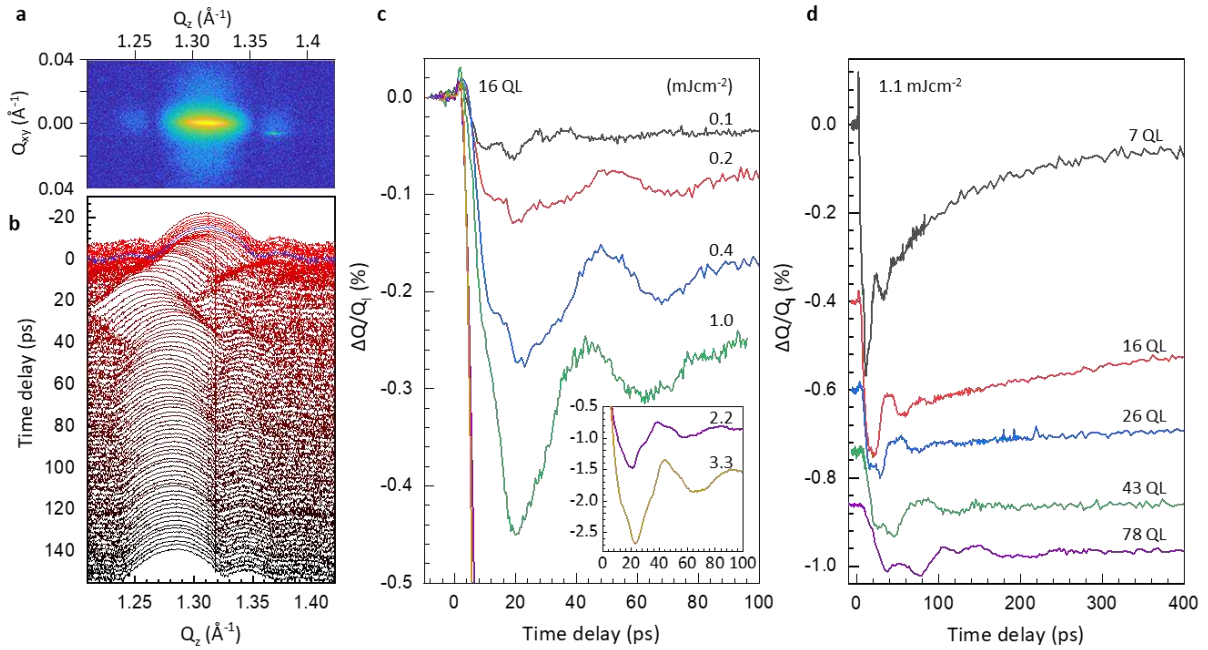


Figure 2. Interlayer vibration modes and relaxation fits to strain curves. (a–b) Position change of the (006) and (015) Bragg peaks in the Q_z and Q_{zy} directions. (c–f) Example strain curve fitting example with a 16 QL sample and 1.1 mJcm^{-2} fluence. (g) The relaxation damping constant τ_{rlx}^1 for 16QL (squares) and 26 QL (circles). The red and blue symbols correspond to the values derived from data obtained at XFEL and the synchrotron source, respectively. (h) τ_{rlx}^2 for 16QL (squares) and 26 QL (circles) derived from data obtained at the synchrotron. (i) The oscillation frequencies for the breathing (red) and interface (blue) modes, for Bi_2Se_3 films with different thicknesses. The error bars denote the 95% confidence intervals. The measured Raman frequencies are plotted as squares. The solid blue line represents the fit to the breathing mode model. (j) The propagation velocities for the breathing mode are plotted as blue circles. The error bars denote the 95% confidence intervals. The triangle and square represent the measurements obtained by Raman spectroscopy (Ref. 30) and ultrafast laser reflection (Ref. 31), respectively.

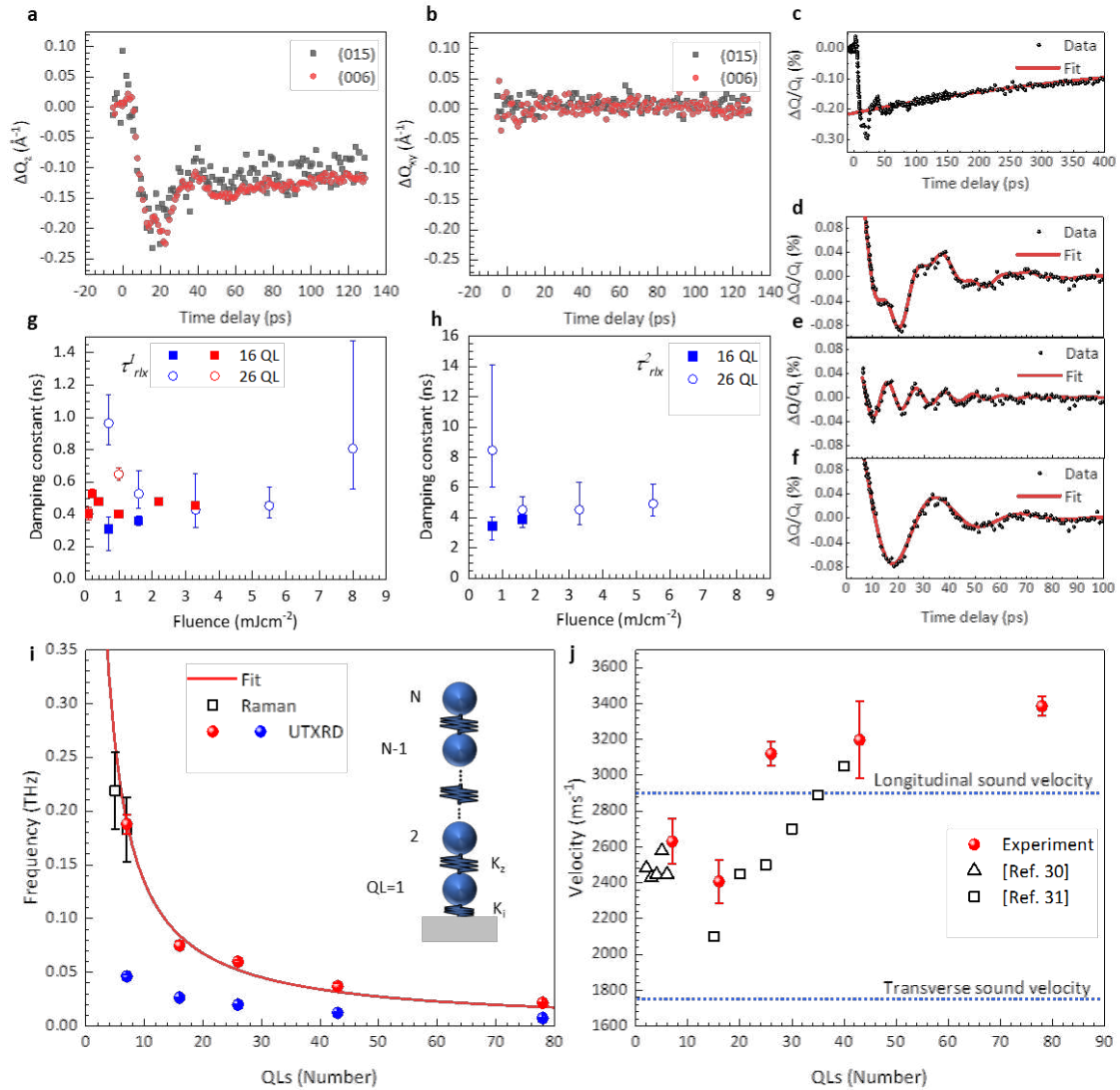


Figure 3. The interlayer contractive strain and maximum expansive strain on a 16 QL Bi_2Se_3 sample. (a) Contractive strain for different fluences up to time delay of 8 ps. The data points (dots) are plotted with the error functions (lines). The maximum contractive strains and their corresponding time delays are plotted as squares and open circles, respectively. (b) The maximum expansive strain as a function of laser fluence for the 16 QL sample from Fig. 1d. The laser fluence ranges from 0.1 to 3.3 mJcm^{-2} . The maximum lattice expansion scales linearly with fluence. The maximum expansive strains were taken as the minima in the strain curves. For each time delay, the centre of mass is averaged over the measurements, and the error bars represent the standard deviation. (c) Compressive strain as a function of time delay for a 1 mJcm^{-2} fluence. The maximum contraction occurred at a time delay of 2.47 ps.

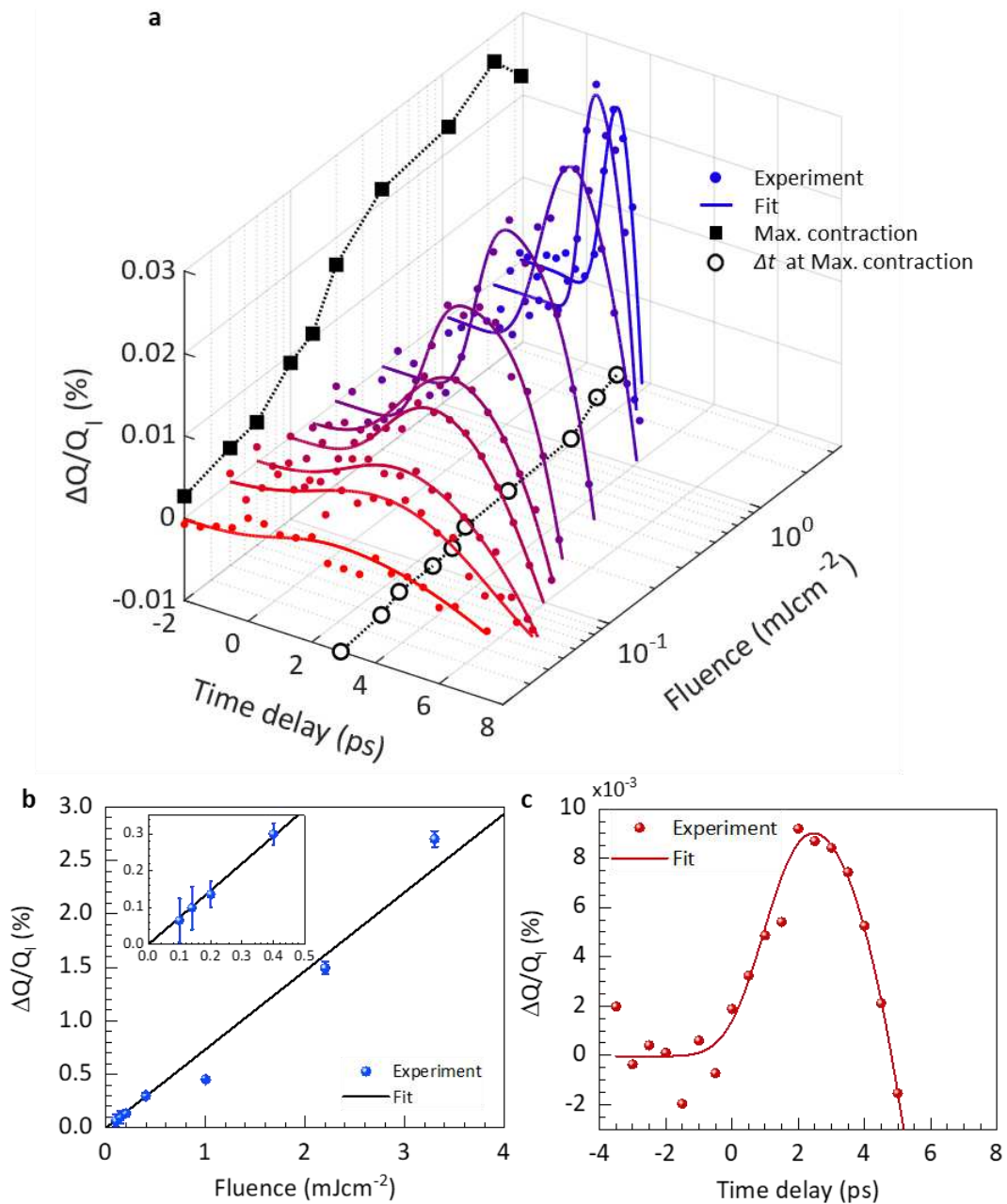


Figure 4. Theoretical analysis of interlayer distance contraction and expansion. (a) The maximum compressive stress is plotted against the carrier density extracted from Fig. 3a (red circle), with the Lifshitz model (line) overlaid. The stress data for carrier densities over 3.564×10^{20} (with 0.4 mJcm^{-2} fluence) were excluded since they were in the saturation regime. The inset shows the entire dataset. (b) The calculated charge density (CD) distribution along the c -axis of the crystal and the atomic configuration in a QL. To display the carrier distribution, we have aligned the y -axis of the CD distribution with the atomic positions. The dashed lines represent the boundaries of the metallic surface in the Lifshitz model. (c) The projected density of states (PDOS) of modulated interlayer distance, Δs , and the corresponding band structure in the vicinity of the Γ point. The coloured lines indicate contributions by atomic orbitals. Band inversion occurs as the interlayer distance expands.

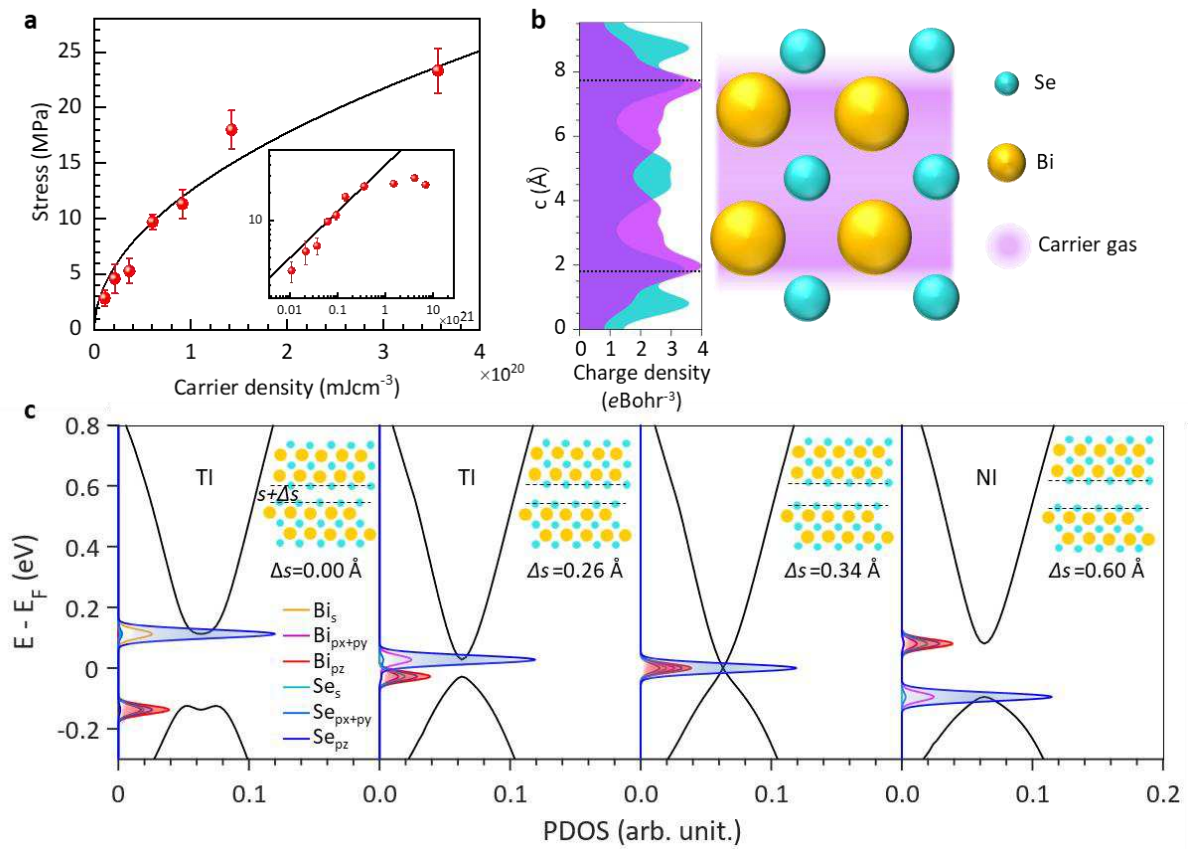


Table 1. K_i values obtained from the results with a simple linear chain model with a nonzero substrate force constant and K_i/K_z ratios.

Thickness (QLs)	7	16	26	43	78
$K_i (\times 10^{18} \text{ Nm}^{-3})$	4.35	3.26	2.98	1.90	1.24
$K_i / K_z (\times 10^{-2})$	8.43	7.67	4.18	2.54	1.48

Figures

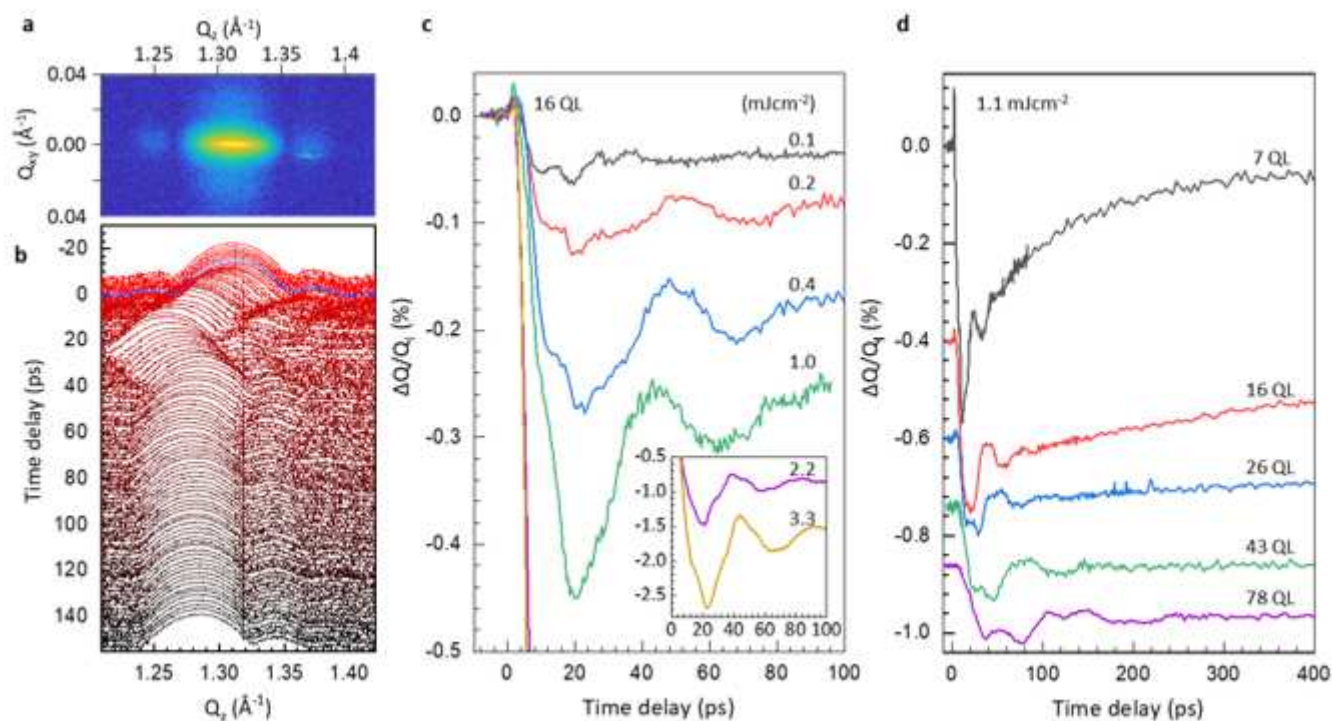


Figure 1

Strain evolution observed at the (006) Bragg peak. (a) The (006) Bragg reflection before laser excitation. (b) In-plane ($\Delta Q_{xy} = 0.08 \text{ \AA}^{-1}$)-averaged (006) Bragg peak after the time delay. The intensity profile at $\Delta t = 0$ is indicated by the blue line. (c) Strain evolution in a 16 QL Bi_2Se_3 film for different laser fluences. Contractive strains are observed between time delays of 0 and 6 ps. The lattice is subsequently released, and the strain rapidly turns expansive and is accompanied by oscillations. (d) Strain evolution in Bi_2Se_3 films with 7, 16, 26, 43, and 78 QLs, at 1.1 mJcm^{-2} fluence.

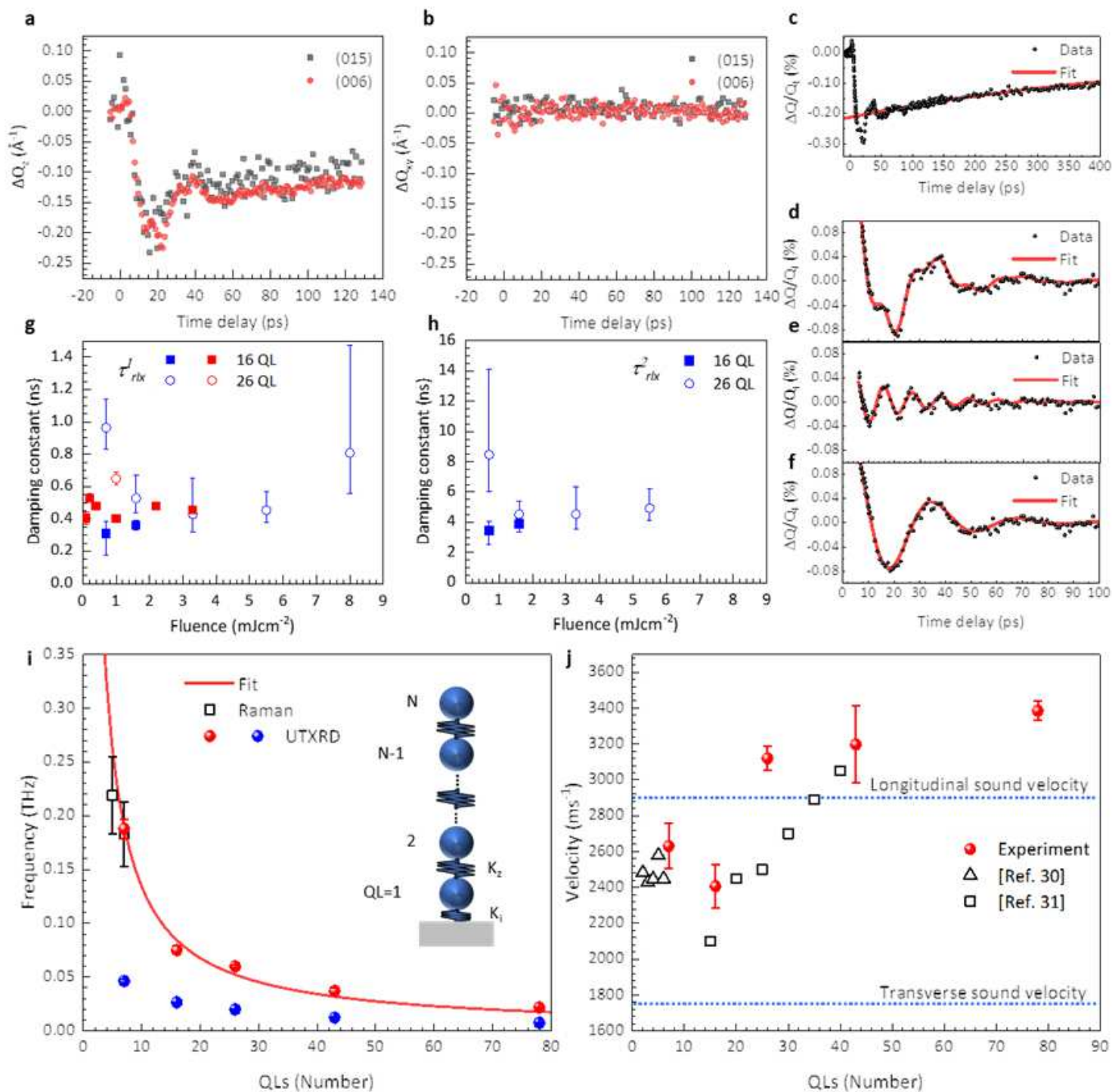


Figure 2

Interlayer vibration modes and relaxation fits to strain curves. (a–b) Position change of the (006) and (015) Bragg peaks in the Qz and Qzy directions. (c–f) Example strain curve fitting example with a 16 QL sample and 1.1 mJ/cm² fluence. (g) The relaxation damping constant τ_{rlx}^{-1} for 16QL (squares) and 26 QL (circles). The red and blue symbols correspond to the values derived from data obtained at XFEL and the synchrotron source, respectively. (h) τ_{rlx}^{-2} for 16QL (squares) and 26 QL (circles) derived from data obtained at the synchrotron. (i) The oscillation frequencies for the breathing (red) and interface (blue)

modes, for Bi₂Se₃ films with different thicknesses. The error bars denote the 95% confidence intervals. The measured Raman frequencies are plotted as squares. The solid blue line represents the fit to the breathing mode model. (j) The propagation velocities for the breathing mode are plotted as blue circles. The error bars denote the 95% confidence intervals. The triangle and square represent the measurements obtained by Raman spectroscopy (Ref. 30) and ultrafast laser reflection (Ref. 31), respectively.

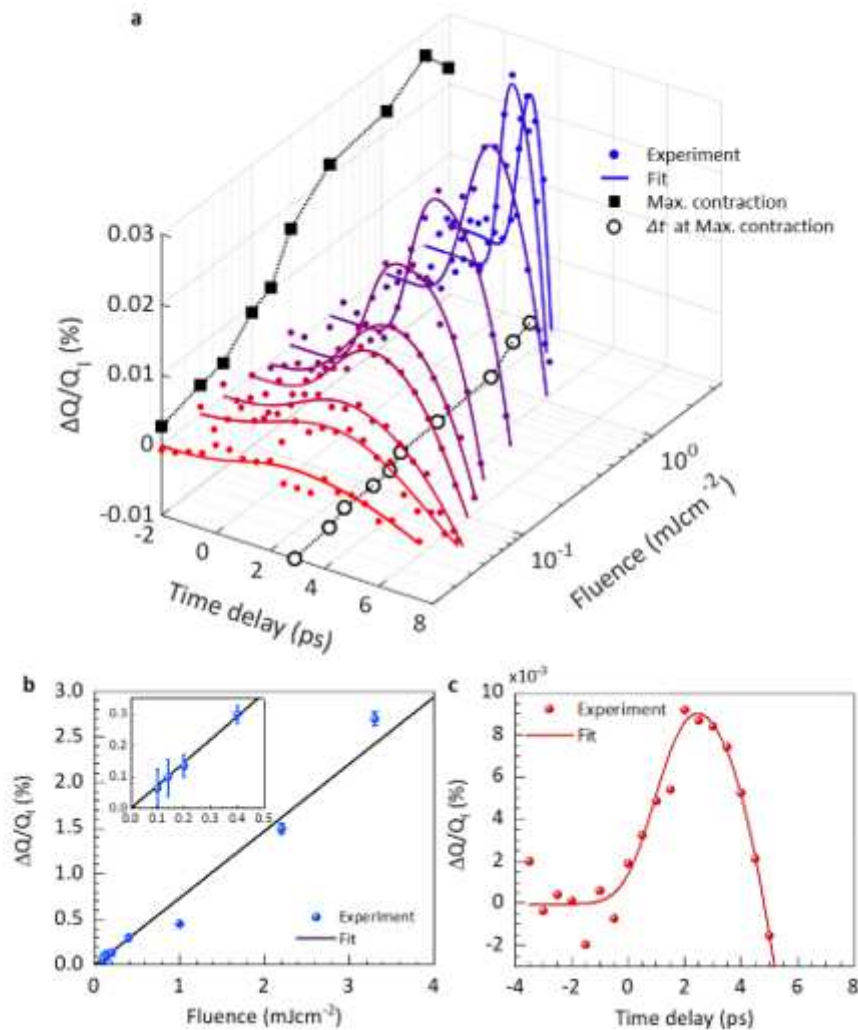


Figure 3

The interlayer contractive strain and maximum expansive strain on a 16 QL Bi₂Se₃ sample. (a) Contractive strain for different fluences up to time delay of 8 ps. The data points (dots) are plotted with the error functions (lines). The maximum contractive strains and their corresponding time delays are plotted as squares and open circles, respectively. (b) The maximum expansive strain as a function of laser fluence for the 16 QL sample from Fig. 1d. The laser fluence ranges from 0.1 to 3.3 mJcm^{-2} . The maximum lattice expansion scales linearly with fluence. The maximum expansive strains were taken as the minima in the strain curves. For each time delay, the centre of mass is averaged over the measurements, and the error bars represent the standard deviation. (c) Compressive strain as a function of time delay for a 1 mJcm^{-2} fluence. The maximum contraction occurred at a time delay of 2.47 ps.

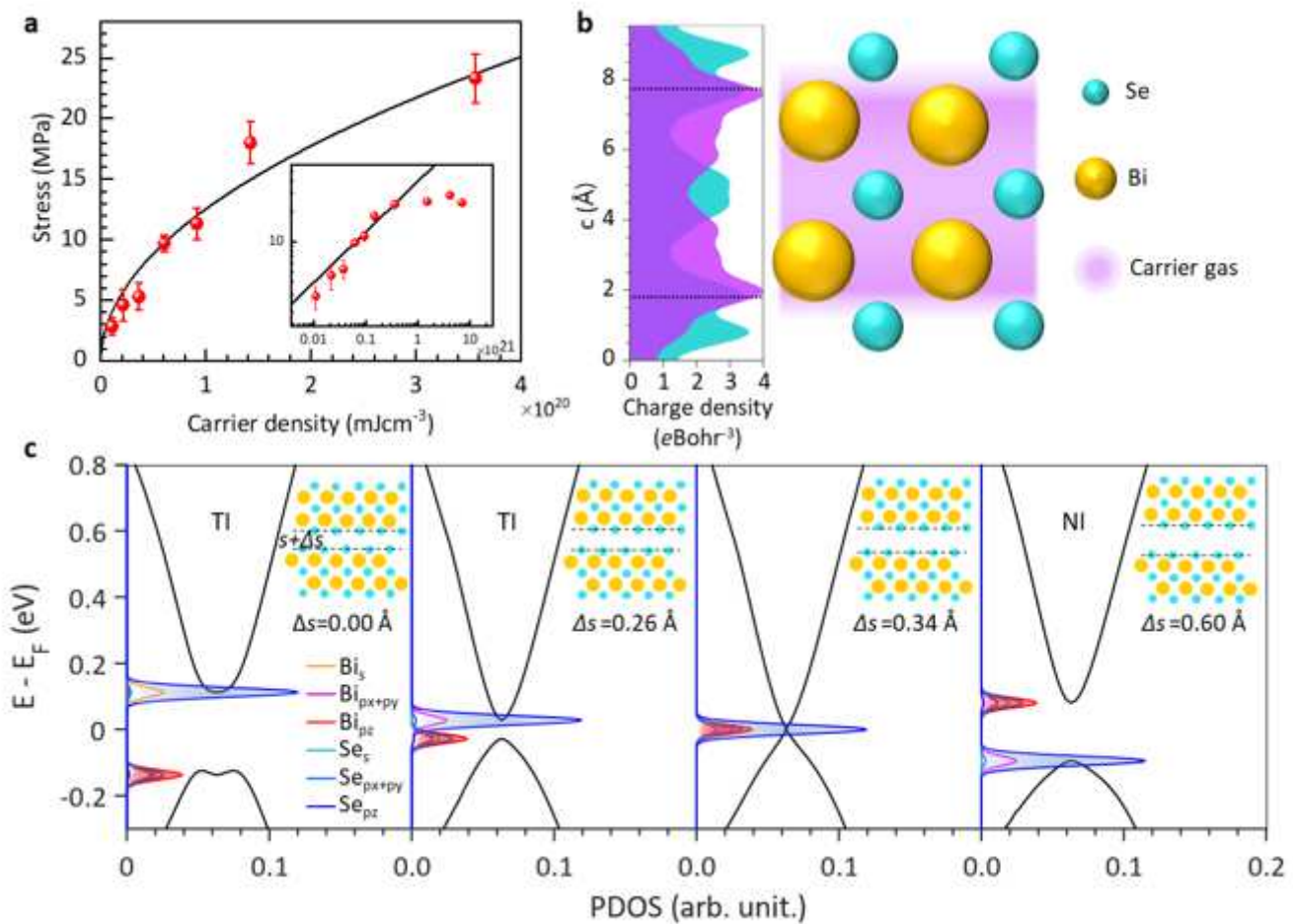


Figure 4

Theoretical analysis of interlayer distance contraction and expansion.

Supplementary Files

This is a list of supplementary files associated with this preprint. Click to download.

- [BiSeSogangSINP.docx](#)